Complex structure and efficient characterization of multiphoton split states in integrated circuits

Jihua Zhang [*] and Andrey A. Sukhorukov [†]

ARC Centre of Excellence for Transformative Meta-Optical Systems, Department of Electronic Materials Engineering,
Research School of Physics, The Australian National University, Canberra, ACT 2601, Australia

Multiphoton split states, where each photon is in a different spatial mode, represent an essential resource for various quantum applications, yet their efficient characterization remains an open problem. Here, we formulate the general structure of their reduced spatial density matrices and identify the number of real and complex-valued independent coefficients, which in particular completely determine the distinguishability of all photons. Then, we show that this density matrix can be fully characterized by measuring correlations after photon interference in a static integrated circuit, where the required number of outputs scales subquadratically versus the number of photons. We present optimized circuit designs composed of segmented coupled waveguides, representing a linear optical neural network, which minimize the reconstruction error and facilitate robustness to fabrication deviations.

I. INTRODUCTION

Multiphoton split states (MPSSs), where each photon is in a different spatial mode of free-space beams, fibers, or waveguides, represent an essential resource for fundamental tests of quantum mechanics and various applications in quantum simulations and computations [1]. For example, many photon interference and distinguishability experiments are based on MPSSs where each photon is injected from a different spatial port [2–8]. Furthermore, photon boson sampling experiments that can demonstrate quantum advantage commonly employ PSS sources that provide multiple indistinguishable photons, with each of the photons injected into a different port of a linear optical network [9–14]. Remarkably, PSSs with more than two photons were recently shown to possess a multiphoton collective phase beyond the real-valued pairwise photon distinguishability measure, opening new degrees of freedom for quantum information [4,15,16]. Therefore, the characterization of PSSs is of great importance from fundamental and practical perspectives.

Importantly, the indistinguishability of all photons in MPSSs cannot be inferred from the distinguishability of constituent photon pairs, which demands characterization based on multiphoton interference. Efficient protocols for witnessing multiphoton indistinguishability were developed and realized with reconfigurable multiport interferometers [7] under the assumption of a specific density-matrix form, whereas it remains an open problem for general states (see the discussion in the Supplemental Material of Ref. [6]).

Beyond the quantification of indistinguishability, the measurement of the full density matrix can provide comprehensive information about the state, including the collective photon phase. This is typically done by a process called quantum state tomography, in which the density matrix of the input quantum state is reconstructed after a series of projection measurements [17–19]. To fully reconstruct the density matrix, the number of distinct measurements which are in the form of multiphoton correlations should exceed the number of free parameters in the density matrix, which increases exponentially with the number of photons [20]. To satisfy this requirement, conventional tomography approaches are based on free-space setups or integrated circuits that are reconfigured multiple times [7,21,22], yet the reconfiguration can be a source of experimental inaccuracies and can also make the characterization time-consuming for larger numbers of photons. On the other hand, static tomography approaches have been suggested [23–27] and realized experimentally [28,29], where the measurements at the outputs of a fixed photonic circuit enable the full-state reconstruction. However, such methods have been developed for general states without taking into account the specific structure of PSSs. An outstanding question of how to perform optimal characterization of PSSs with the minimum number of measurements and high robustness to fabrication inaccuracy and measurement noise while using the most compact and practical photonic circuit design remains.

In this work, we formulate the general properties of the spatial density-matrix structure for the PSSs without any assumptions. Then, we present a scalable approach for a single-shot complete state measurement with a static integrated photonic circuit, without the need for reconfigurability. Specifically, we first theoretically derive the number of free parameters and the structure of the reduced spatial density matrix as a function of the number of photons. Furthermore, we obtain the number of free real and imaginary parts, in which the imaginary values of the density matrix are associated with the multiphoton collective phases. To realize the state tomography, we propose a multiport coupled waveguide array that is segmented into multiple sections along the propagation

[*]jhzhanghust@gmail.com
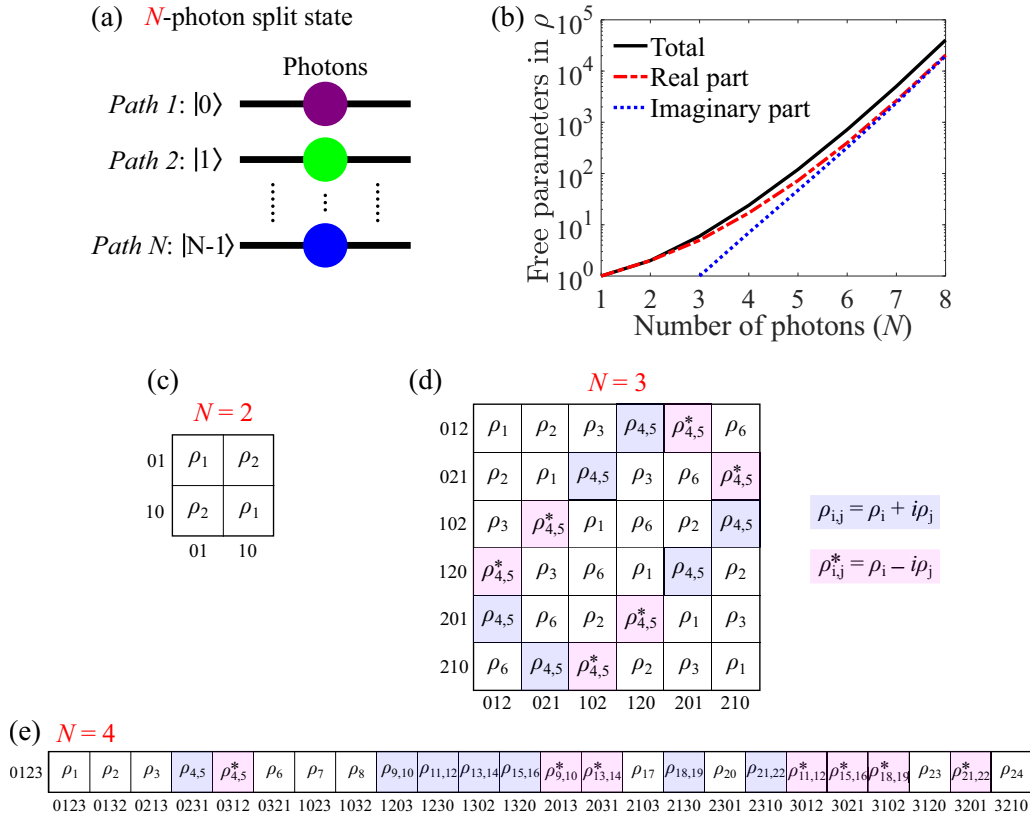
[†]andrey.sukhorukov@anu.edu.au

FIG. 1. (a) Schematic of the N-photon split state (NPSS) where each photon is located in a different spatial mode or path. (b) Number of real, imaginary, and total independent parameters in the reduced spatial density matrix of NPSS as a function of the number of photons. The structure of the reduced spatial density matrices for (c) 2PSSs and (d) 3PSSs. The elements without and with backgrounds are purely real and complex valued, respectively. Note that only the nonzero elements of the full density matrix (dimension: $N^N \times N^N$) are shown. (e) First row of the nonzero elements of the 4PSS density matrix. Other rows will have the same elements in different orders.

direction with the specially introduced local phase shifts between adjacent sections. Such a configuration effectively represents a photonic neural network (NN), where the waveguide coupling and local phase shifts function as the weight and bias, respectively. By optimizing the photonic circuit, we identify the configurations allowing for the most efficient tomography of two-, three-, and four-photon split states with reduced sensitivity to measurement noise and fabrication deviations. Different from previous reconfigurable platforms which require multiple measurements with an exponential increase in the number of photons, the proposed scheme can realize the tomography in a single shot without reconfigurability. When this scheme is compared with previous static approaches developed for general states, the performance is better, and the complexity of the photonic circuit is reduced. This makes the proposed scheme scalable to larger photon numbers.

This paper is organized as follows. In Sec. II, we formulate the general structure of the reduced spatial density matrix for PSSs after tracing out the internal spectral degree of freedom and determine the numbers of independent real- and complex-valued coefficients as a function of the number of photons. In Sec. III, we introduce a circuit design based on coupled waveguides, representing a linear artificial neural network, and describe its application for split-state tomography. Then, in Sec. IV, we present the circuit designs for two-, three-, and

four-photon split states, optimized for accurate state reconstruction in the presence of measurement noise or fabrication imperfections. Finally, we present the conclusions and outlook in Sec. V

II. MULTIPHOTON SPLIT STATES AND THE SPATIAL DENSITY MATRIX

We define a multiphoton split state formed by N photons where each photon is located on a different spatial path, with orthogonal states labeled by $|0\rangle, |1\rangle, \ldots, |N-1\rangle$, as shown in Fig. 1(a). The frequency-dependent wave function of such a PSS can be expressed as

$$
\begin{aligned}
|\Psi\rangle = \int d\omega_0 d\omega_1 \cdots d\omega_{N-1} \psi(\omega_0, \omega_1, \ldots, \omega_{N-1}) \\
\times \hat{a}_0^\dagger(\omega_0)\hat{a}_1^\dagger(\omega_1) \cdots \hat{a}_{N-1}^\dagger(\omega_{N-1})|0\rangle,
\end{aligned} \tag{1}
$$

where $\psi(\omega_0, \omega_1, \ldots, \omega_{N-1})$ is the joint spatial and spectral distribution of N photons. Note that $|0\rangle$ in Eq. (1) stands for the photon vacuum state instead of the spatial mode of the first path mentioned earlier.

We consider setups using commonly available single-photon click detectors. The coincidences of signals from several detectors then provide a measure of the photon correlations. While the photons might have different

internal structures, such as frequency spectra, the conventional detectors register the arrival time only within specific time bins. Such detection and correlation measurements in photonic circuits do not distinguish the photons by their spectral properties [22,30]. Also, experiments can realize multiphoton interference that does not explicitly depend on the internal structure of photons [4,16,28,29], and such transformations are mathematically described by a unitary operator that mixes different input ports but does not depend on frequency spectra of photons [15,31]. In addition, the single-photon click detectors cannot resolve the number of photons that arrived at the detector.

For the case in which the experimental detectors do not distinguish the photons by their spectrum, a PSS can be characterized by a reduced density matrix, where the internal spectrum degree of freedom of the photons is traced out via integration. In the reduced spatial density matrix, which has dimensions of $N^N \times N^N$, each element is determined by [28]

$$\rho_{s'_0, s'_1, \ldots, s'_{N-1}; s_0, s_1, \ldots, s_{N-1}} = \text{Tr}\big(\hat{\rho} \, \hat{O}_{s'_0, s'_1, \ldots, s'_{N-1}; s_0, s_1, \ldots, s_{N-1}} \big), \quad (2)$$

where $\hat{\rho} = |\Psi\rangle\langle\Psi|$ is the full density matrix and the N-photon density-matrix projection operator is defined as

$$
\begin{aligned}
\hat{O}&_{s'_0, s'_1, \ldots, s'_{N-1}; s_0, s_1, \ldots, s_{N-1}} \\
&= \frac{1}{N!} \int d\omega_0 d\omega_1 \cdots d\omega_{N-1} \hat{a}^\dagger_{s'_0}(\omega_0) \hat{a}^\dagger_{s'_1}(\omega_1) \\
&\quad \times \cdots \hat{a}^\dagger_{s'_{N-1}}(\omega_{N-1}) |0\rangle \\
&\quad \times \langle 0 | \hat{a}_{s_0}(\omega_0) \hat{a}_{s_1}(\omega_1) \cdots \hat{a}_{s_{N-1}}(\omega_{N-1}).
\end{aligned}
\quad (3)
$$

For a split state, the nonzero density-matrix elements can be associated with only indices $(s'_0, s'_1, \ldots, s'_{N-1})$ and $(s_0, s_1, \ldots, s_{N-1})$, which are permutations in the set $(0, 1, \ldots, N-1)$ without repetitions. We also note that the reduced density matrix is invariant under the simultaneous exchange of indices $s'_i \leftrightarrow s'_j$ and $s_i \leftrightarrow s_j$ for arbitrary i and j since the photons are indistinguishable after the internal spectrum degree of freedom is traced out. Using this property, we can map all the elements to just the first row of the density matrix with elements $\rho_{0,1,\ldots,N-1,s_0 s_1 \cdots s_{N-1}}$, where $(s'_0, s'_1, \ldots, s'_{N-1}) = (0, 1, \ldots, N-1)$. Therefore, the number of nonzero and independent elements of the spatial density matrix is the number of permutations of $(s_0, s_1, \ldots, s_{N-1})$ in the set $(0, 1, \ldots, N-1)$ without repetition, which is $N!$. Note that here we are considering un-normalized density matrices, whose elements are proportional to correlations measured over a specific time interval, as discussed in the following. A conventional normalization with $\text{Tr}(\hat{\rho}) = 1$ can be performed only after a reconstruction by dividing all the matrix elements by $(\rho_1 N!)$. Importantly, whereas such a normalized matrix will have the number of free parameters reduced by one, i.e., $N! - 1$, all $N!$ parameters need to be considered in the tomographic reconstruction procedure since the normalization factor is not known *a priori*.

Within this formulation, we can associate the appearance of the collective multiphoton phase [15] with the presence of complex-valued density-matrix elements. Since the ordering of $|0\rangle\langle s_0|, |1\rangle\langle s_1|, \ldots, |N-1\rangle\langle s_{N-1}|$ does not affect the

values of density-matrix elements, we have

$$
\begin{aligned}
\rho_{0,1,\ldots,N-1; s_0, s_1, \ldots, s_{N-1}} &= \rho_{q_0, q_1, \ldots, q_{N-1}; 0, 1, \ldots, N-1} \\
&= \rho^*_{0,1,\ldots,N-1; q_0, q_1, \ldots, q_{N-1}},
\end{aligned}
\quad (4)
$$

where $(s_0, s_1, \ldots, s_{N-1})$ is reordered into $(0, 1, \ldots, N-1)$ and $(q_0, q_1, \ldots, q_{N-1})$ is the new order from $(0, 1, \ldots, N-1)$ after the same permutation operation. When $(q_0, q_1, \ldots, q_{N-1}) \equiv (s_0, s_1, \ldots, s_{N-1})$, then it follows from Eq. (4) that $\rho_{0,1,\ldots,N-1; s_0, s_1, \ldots, s_{N-1}} = \rho^*_{0,1,\ldots,N-1; s_0, s_1, \ldots, s_{N-1}}$; that is, this element is real valued. Let us denote the number of such cases by A_N. The remaining $N! - A_N$ elements will have complex values and include $(N! - A_N)/2$ complex-conjugate pairs. Correspondingly, the numbers of independent real and imaginary parts of the density matrix are $(N! + A_N)/2$ and $(N! - A_N)/2$, respectively, resulting in a total of $N!$ real-valued free parameters. We prove that A_N satisfies the recurrence relation $A_N = A_{N-1} + (N-1)A_{N-2}$ for $N \geqslant 3$, with $A_1 = 1$ and $A_2 = 2$; see Appendix A for the derivation.

We show in Fig. 1(b) the number of total, real, and imaginary independent parameters of the split-state density matrix as a function of the number of photons. For $N = (2, 3, 4)$, there are $(2, 6, 24)$ total, $(2, 5, 17)$ real, and $(0, 1, 7)$ imaginary parameters. The corresponding structures of the reduced density matrices are presented in Figs. 1(c)–1(e). We label the independent real and imaginary coefficients with single sequential indices. Figures 1(c) and 1(d) illustrate that one row contains all the different elements, and we show just the first row for a four-photon split state (4PSS) in Fig. 1(e) to save space. Notably, the imaginary parts can appear only for three or more photons ($N \geqslant 3$), in agreement with the properties of the multiphoton collective phase [4,15,16].

We emphasize that the number of independent density-matrix parameters for split states $N!$ is much smaller than that for the general states [28]. This allows for the efficient tomography of split states by taking into account their structure, as we discuss in the following.

III. INTEGRATED CIRCUIT FOR SPLIT-STATE MEASUREMENTS

We now analyze how the characterization of split states can be performed by adopting a static tomography approach [23–29]. We consider an N-input-M-output waveguide circuit where the N input photons interfere, and the N-photon correlations are measured between different combinations of the M output ports, as schematically shown in Fig. 2(a). We analyze the case of the commonly available click detectors that do not distinguish the photons and do not resolve between single- and multiphoton events, such that one can count only the cases when all N photons are detected at N distinct output ports, with the corresponding number of different combinations C_M^N [28]. To realize the state tomography without reconfigurability, the number of different N-photon correlation measurements at the output should exceed the number of unknown density-matrix elements $N!$, that is,

$$C_M^N = \frac{M!}{N!(M-N)!} \geqslant N!. \quad (5)$$

The required minimum number of waveguides M grows linearly up to five-photon states, $M_{\min} = 2N - 1$ for $N \leqslant 5$.
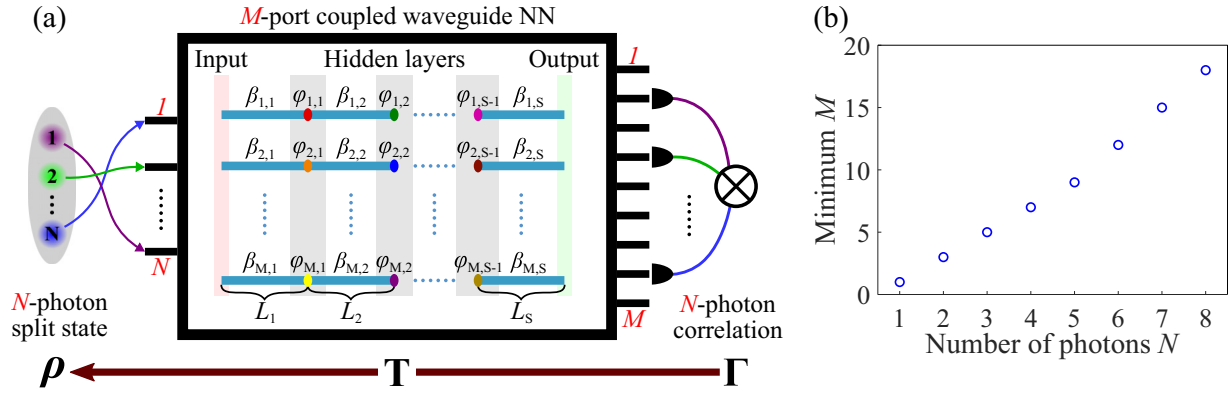
FIG. 2. (a) Schematic of the proposed M-port coupled waveguide neural network for N-photon split state tomography, where the output N-photon correlations enable the reconstruction of the input density matrix. (b) Required number of waveguides for different photon numbers.

For larger photon numbers, we obtain an exact quadratic fitting as $M_{\min} = \lceil 0.139N^2 + 1.174N - 0.387 \rceil$ for $N \leqslant 30$ [see Fig. 2(b)]. We confirm the quadratic scalability at high photon numbers using Stirling's approximation, which provides the asymptotic estimate $M > (N/e)^2 \simeq 0.135N^2$ for $N \gg 1$.

For comparison, if the detectors can resolve the number of photons, the number of different measurable N-photon correlations is determined as combinations with repetitions C_{M+N-1}^N. By substituting this expression in the left-hand side of the inequality in Eq. (5), we find that $M_{\min} = N$ for $N \leqslant 5$ and $M_{\min} = \lceil 0.139N^2 + 0.168N + 0.636 \rceil$ for $N \leqslant 25$. We see that a smaller number of output waveguides may be required in the case of photon-number-resolving detectors, although the scaling is similarly subquadratic as that for simple click detectors. We consider the click detectors in the following, whereas our approach could be applied in the future to optimize photonic circuits for number-resolving detectors when they become widely available.

Since no structure tunability is required, there is a large design freedom of the input-to-output transformation based on integrated waveguide circuits. We demonstrate the general approach of split-state tomography for the realization based on arrays of straight coupled waveguides [32–34] where the undesirable bending losses are absent since higher transmission is critical for the observation of multiphoton interference [35]. Furthermore, the continuous interwaveguide coupling along the propagation direction can make the circuit more compact than the commonly used scheme of cascaded Mach-Zehnder interferometers [12,36] while allowing for the realization of various quantum logic operations [37].

The proposed waveguide circuit is sketched inside the central frame in Fig. 2(a). It consists of M waveguides whose optical modes are coupled to the nearest neighbors with the constant coupling coefficient κ. The waveguides are segmented into S sections with lengths $(L_1, L_2, \ldots, L_S)$. We consider the presence of tailored phase shifts $\varphi_{i,j}$ at the interfaces between adjacent sections, noting that such localized shifts were demonstrated experimentally [38] and their incorporation was predicted to allow arbitrary unitary transformations [33,39]. In addition, the design based on straight and identical waveguides ensures that there is no mismatch in the photon propagation lengths and dispersion, and the circuit

is expected to better preserve the degree of photon indistinguishability during their interference compared to cascaded interferometers [40]. By design, the losses are expected to be similar for all waveguides, and we assume in the following that the output multiphoton correlations are above the noise level [35], which can be satisfied experimentally for at least $N = 5$ photons [40]. Essentially, the configuration in Fig. 2(a) represents a linear artificial neural network [41] with $S - 1$ hidden layers, where each hidden layer has M neurons. The waveguide couplings in each section function as the weights, and the local phase shifts play roles similar to the bias.

The overall linear system transformation of the multiphoton state, provided that the losses are negligible, can be determined by a classical or one-photon unitary transfer matrix,

$$\mathbf{U} = \mathbf{W}_S \, \mathbf{B}_{S-1} \, \mathbf{W}_{S-1} \, \cdots \, \mathbf{B}_2 \, \mathbf{W}_2 \, \mathbf{B}_1 \, \mathbf{W}_1 \,. \qquad (6)$$

Here, $\mathbf{W}_j = \exp(i\mathbf{C}L_j)$, calculated through the matrix exponent, is the weight matrix of layer j, where the coupling matrix elements are $\mathbf{C}_{n,m} = \kappa \delta_{n,m\pm1}$. The bias matrix acting on the jth hidden layer is $\mathbf{B}_j = \exp(i\Phi_j)$, where the exponent is applied elementwise to the phase-shift matrix $\Phi_j = \mathrm{diag}(\varphi_{1,j}, \varphi_{2,j}, \ldots, \varphi_{M,j})$. The $M \times M$ unitary matrix $\mathbf{U}$ can be flexibly tuned by varying the lengths of sections and local phase shifts.

For an N-photon split state, where the photons are coupled to specific N ports at the input, its transformation is governed by the N-in-M-out matrix $\mathbf{U}_r$, which contains N columns of $\mathbf{U}$ corresponding to the selected inputs. The density matrix of the state at the output is $\hat{\rho}_{\mathrm{out}} = [\otimes_{n=1}^N \mathbf{U}_r] \, \hat{\rho} \, [\otimes_{n=1}^N \mathbf{U}_r]^\dagger$, which has an extended dimension of $M^N \times M^N$. Then, we calculate the output N-photon correlations, which correspond to the diagonal terms of $\hat{\rho}_{\mathrm{out}}$ and depend on the transfer matrix $\mathbf{U}_r$ and all the elements of the input density matrix $\hat{\rho}$. The magnitudes of output N-photon correlations can be represented by a vector $\vec{\Gamma}$ whose length is equal to different combinations $C_M^N = M!/[N!(M - N)!]$. The correlations can be expressed through the independent elements of the input density matrix arranged in a vector $\vec{\rho}_{\mathrm{free}}$ of length $N!$ [28,29],

$$\vec{\Gamma} = \mathbf{T} \, \vec{\rho}_{\mathrm{free}} \,, \qquad (7)$$

where the matrix **T** is determined by $\mathbf{U}_r$ and the structure of the split-state density matrix.

Finally, we can reconstruct the input density matrix based on the measured N-photon correlations as

$$\vec{\rho}_{\text{free}} = \mathbf{T}^+ \vec{\Gamma},\qquad(8)$$

where $\mathbf{T}^+$ is the pseudoinverse of **T**.

It is essential to optimize the integrated circuit to reduce the reconstruction sensitivity to noise and measurement errors. Mathematically, this is achieved by minimizing the condition number of the matrix **T**, defined as the ratio of the transformation's maximum and minimum singular values $\sigma_{\max}(\mathbf{T})/\sigma_{\min}(\mathbf{T})$ [42]. For our structure design, we perform numerical optimization of the waveguide section lengths and the local phase shifts based on the Nelder-Mead simplex direct search algorithm realized using the FMINSEARCH function in MATLAB.

IV. RESULTS AND DISCUSSION

We performed extensive simulations of coupled-waveguide neural networks and found that the tomography of split states with a photon number of at least up to four can be efficiently performed in structures in which all sections have the same length, all waveguides have the same propagation constants and thus zero detunings, and all the near-neighbor waveguide couplings are equal to each other. These conditions make the photonic circuit design and fabrication simpler, where all the waveguides have the same widths and the spacings between them are identical. We show in the following that optimization of the local phase shifts and the total waveguide length L allows us to reach low condition numbers, corresponding to low sensitivity to noise during the reconstruction. To simplify the notations, we consider the scaling of the waveguide length in the units of κ^{-1}, such that the coupling coefficient is normalized to 1.

We first analyze the tomography of 2PSSs. We choose the minimum required number of $M=3$ waveguides according to Eq. (5) and Fig. 2(b), select the first and third waveguides as the input ports, and consider a circuit structure with one hidden layer ($S=2$), as sketched in Fig. 3(a). We perform the optimization for different waveguide lengths and show the best condition number values in Fig. 3(b). We can see that the condition number reaches a minimum value of $\simeq2.3$ when the waveguide length is longer than 0.84. This optimized condition number is smaller than the previously reported values for tomography of general two-photon states [26,28]. The corresponding optimized phase shifts at the hidden layer are shown in Fig. 3(c), where we assign zero to one of the phases since the global phase does not affect the output correlations. Interestingly, all three phase shifts are zero for a waveguide length shorter than 0.84, which effectively corresponds to the absence of a hidden layer. For longer waveguides, the minimum value of the condition number is achieved for circuits with an optimal hidden layer. For comparison, Fig. 3(d) shows the condition number for a structure without a hidden layer. We see that the circuit can allow for optimal performance over a broad range of structure lengths, offering more flexibility in integrating with other photonic components.
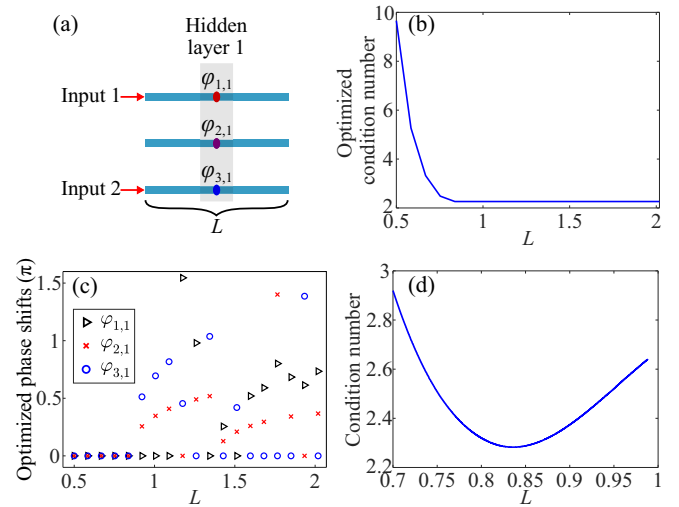

FIG. 3. Optimized circuit for 2PSS tomography. (a) The structure of three coupled waveguides with one hidden layer. Optimized (b) condition number and (c) phase shifts at the hidden layer as a function of the total waveguide length. (d) Condition number for a structure without a hidden layer vs the waveguide length.

Next, we investigate the 3PSS tomography. Then, we use Eq. (5) to determine the required number of waveguides as $M=5$ and choose the first, third, and fifth waveguides as the input ports; see an illustration in Fig. 4(a). We check that without hidden layers, the condition number is very high, which would prevent state reconstruction. The condition
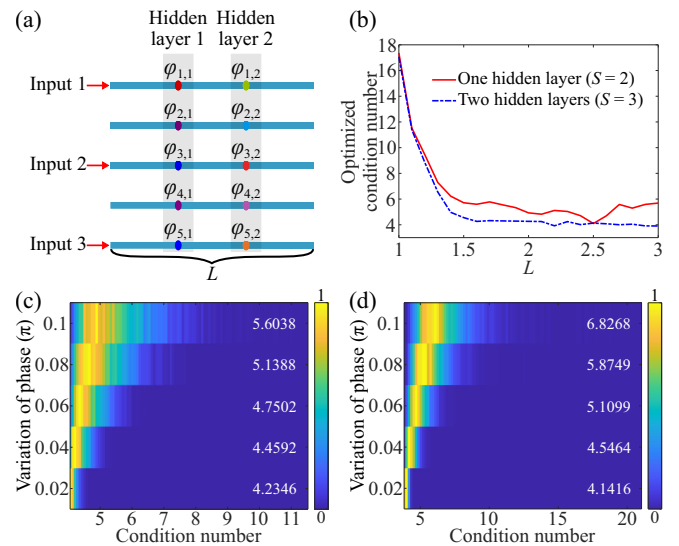

FIG. 4. Tomography of a 3PSS. (a) The structure of the 3-in-5-out coupled-waveguide network with two hidden layers. (b) Optimized condition numbers vs the total waveguide length with one or two hidden layers. Normalized probability density of condition number values for 5000 simulations with random variations of the phase shifts from the optimal values for structures with (c) one hidden layer ($S=2$, $L=2.5$) and (d) two hidden layers ($S=3$, $L=3$). The vertical axis represents the magnitude of the random variations, and the white numbers are the corresponding averaged condition numbers.

number dependences on the structure length with the optimized one or two hidden layers are presented in Fig. 4(b). Overall, for a certain length, more hidden layers can provide lower condition numbers because there are more tuning parameters. The smallest condition numbers are $\simeq 4.1$ at $L = 2.5$ and $\simeq 3.9$ at $L = 3$ for one and two hidden layers, respectively. These values are much smaller than the ones for general three-photon states [43]. The corresponding optimized phase shifts are $\varphi_{j,1} = (0, 1.083, 1.167, 0.973, 5.509)$ for one hidden layer and $\varphi_{j,1} = (0, 4.248, 3.808, 1.442, 5.098)$ and $\varphi_{j,2} = (0, 1.844, 1.948, 2.988, 4.155)$ for two hidden layers.

We confirm the practicality of the designs by quantifying the tolerance of the optimal structures for 3PSS tomography to variations of the phase shifts due to potential fabrication errors. Figures 4(c) and 4(d) show the normalized probability density of the condition number values for random deviations of the phase shifts from the optimal values in different variation ranges. The white numbers are the average condition numbers for different variation magnitudes. At small deviations, the structure with two hidden layers performs better with the smaller condition number. In the case of phase-shift variations of $0.04\,\pi$ or larger, the structure with one hidden layer is better. This is because there are fewer phase shifts, and the performance is more robust to their variations. Overall, the condition numbers are smaller than 7, even when the phase shifts vary from the optimized values by a magnitude up to 0.1π. This confirms the high fabrication tolerance of the circuits. Next, we numerically demonstrate the density-matrix reconstruction of 3PSSs. As an example, we consider the 3PSS composed of photons with uncorrelated frequency spectra, defined by the wave function $|\Psi\rangle = \int d\omega_0 d\omega_1 d\omega_2 \phi_0(\omega_0)\phi_1(\omega_1)\phi_2(\omega_2)\hat{a}_0^\dagger(\omega_0)\hat{a}_1^\dagger(\omega_1)\hat{a}_2^\dagger(\omega_2)|0\rangle$, where $\phi_j(\omega)$ represents the spectral wave function of one photon in the jth spatial path. In simulations, we assume the pairwise spectral overlaps are $\langle\phi_0|\phi_1\rangle = 0.7e^{-i\pi/3}$, $\langle\phi_1|\phi_2\rangle = 0.65$, and $\langle\phi_2|\phi_0\rangle = 0.6$, which define all the spatial density-matrix elements and the three-photon collective phase of $-\pi/3$ as formulated in Appendix B. The real and imaginary parts of the density matrix of this state are presented in Figs. 5(a) and 5(b), respectively. Figures 5(c) and 5(e) show the predicted three-photon correlation probabilities at the output of the optimized circuits with one and two hidden layers, respectively. We see that the correlations are different for each structure. Based on the output correlations, one can reconstruct the input density matrix. In order to verify the low sensitivity to the measurement noise, we apply a Gaussian noise to the correlations and use them to reconstruct the input density matrix. We quantify the quality of the tomography procedure by the fidelity between the reconstructed ($\rho_{\rm rec}$) and input ($\rho_{\rm th}$) density matrices, defined as $\mathrm{Tr}(\sqrt{\sqrt{\rho_{\rm th}}\rho_{\rm rec}\sqrt{\rho_{\rm th}}})$. Figures 5(d) and 5(f) show the corresponding statistical distributions of the reconstruction fidelity for 5000 simulations when a Gaussian noise with a standard deviation of 5% is added to the predicted correlation probabilities. We find that the fidelity stays above 0.95 for both one- and two-hidden-layer structures, with average values of $\simeq 0.99$. We also confirm similarly high fidelity for different 3PSSs, including those with zero collective phase. These results indicate the high accuracy of the tomographic reconstruction of split states in the presence of measurement noise.
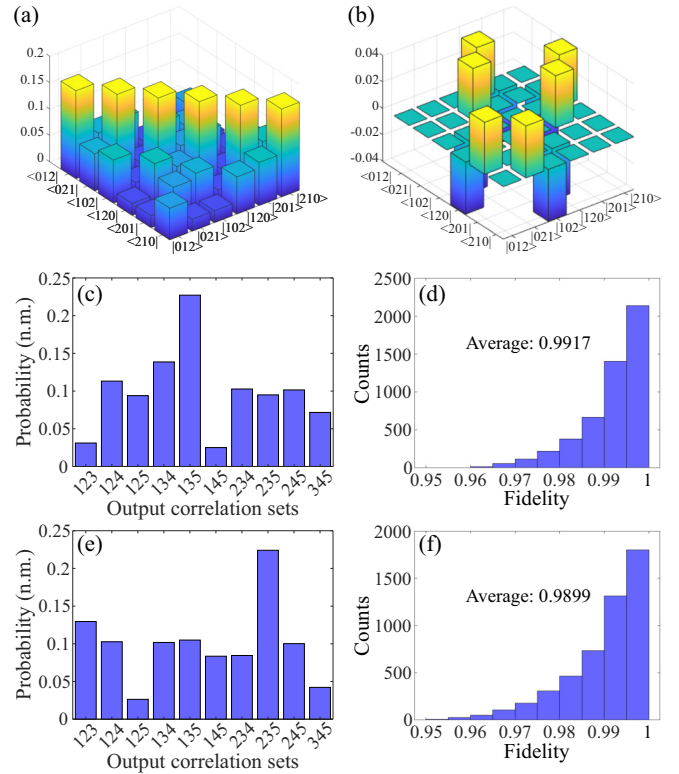

FIG. 5. Three-photon reconstruction fidelity in the presence of measurement noise. (a) Real and (b) imaginary parts of the density matrix for an input three-photon split state with a collective phase of $-\pi/3$. (c) and (e) The predicted three-photon correlation probabilities after passing through the optimized waveguide network. (d) and (f) The statistical distribution of the density-matrix-reconstruction fidelity for 5000 simulations when a Gaussian noise with a standard deviation of 5% is added to the output correlations. Results correspond to the structures with (c) and (d) one and (e) and (f) two hidden layers.

The proposed approach and its high tolerance of fabrication errors and shot noise are also applicable to a larger number of photons. For example, we numerically designed a circuit with $N = 4$, $M = 7$, $S = 3$, and $L = 3$ for the tomography of a 4PSS with an optimized condition number of 16.3464 for the hidden-layer phase shifts $\varphi_{j,1} = (0, 1.126, 0.306, 4.331, 4.990, 1.633, 2.419)$ and $\varphi_{j,2} = (0, 1.212, 1.998, 2.246, 0.371, 6.002, 0.894)$.

The designed circuits can be realized experimentally based on different integrated photonic platforms with established fabrication techniques. The localized phase shifts in coupled segmented waveguides were achieved through femtosecond-laser writing in silica [38], and phase control using voids inside the waveguide was shown in silicon photonic circuits [44]. The practical difficulty lies in the preparation of high-quality multiphoton states and processing of correlation measurements, with the latter task scaling exponentially with N. State-of-the-art experiments have reached up to five photons with reconfigurable multiport interferometers [40]. Since our method uses a static circuit, one can measure all $N!$ multiphoton correlations simultaneously, offering a speedup compared with the previous reconfigurable setups, and

therefore, our approach is expected to perform well for up to five and potentially larger numbers of photons.

V. CONCLUSION

To conclude, we formulated the general structure of the spatial density matrix for multiphoton split states, which are an important resource for various quantum applications and whose resource-efficient characterization is a sought-after capability. We then proposed a coupled waveguide array forming a photonic neural network for the quantum tomography of such states with low sensitivity to noise and high tolerance of fabrication errors. The state measurement can be performed using a static photonic circuit, and this approach is scalable to high photon numbers.

We anticipate that the proposed platform, enabling simple and robust characterization of such commonly used quantum states, will stimulate further developments and applications of quantum optical circuits, such as characterizing the indistinguishability of multiple photons and multiphoton collective phases. In particular, since our scheme does not require reconfigurability, it is especially suitable for integration with on-chip superconducting nanowire single-photon detectors operating at cryogenic temperatures to facilitate plug-and-play split-state measurements. Furthermore, the theoretical methodology can be extended to split states where photons are separated not only in spatial ports but also in other degrees of freedom, such as polarization and orbital angular momentum.

The simulation data underlying the results presented in this paper may be obtained from the authors upon request.

APPENDIX A: NUMBER OF REAL AND IMAGINARY FREE PARAMETERS IN THE DENSITY MATRICES OF SPLIT STATES

As derived in the main text, the number of nonzero elements in the reduced density matrix of an N-photon split state equals the distinct projection operators in the form of Eq. (3), and it is $N!$. The numbers of real and imaginary parts are determined by the numbers of nonzero distinct $(\hat{O} + \hat{O}_{\mathrm{H.c.}})/2$ and $(\hat{O} - \hat{O}_{\mathrm{H.c.}})/2$, respectively, where H.c. stands for the Hermitian conjugate [28]. To perform the counting, we define by A_N the number of cases when $\hat{O} = \hat{O}_{\mathrm{H.c.}}$, such that the related imaginary parts are zero. A_N is essentially the number of permutations in the symmetric group of N elements which are autoinverse to themselves. Next, we derive the recurrence relation for A_N as a function of N. Let us consider the value of s_{N-1}. When $s_{N-1} = N - 1$, the number of cases where $\hat{O} = \hat{O}_{\mathrm{H.c.}}$ is A_{N-1}. When $s_{N-1} = \tilde{n}$ for $\tilde{n} = (0, 1, \ldots, N - 2)$, the condition $\hat{O} = \hat{O}_{\mathrm{H.c.}}$ can be satisfied only when $s_{\tilde{n}} = N - 1$. In this case, the number of cases where $\hat{O} = \hat{O}_{\mathrm{H.c.}}$ becomes A_{N-2}. Since $\tilde{n}$ can take $N - 1$ values, the total number is $(N - 1)A_{N-2}$. Therefore, we obtain the relation

$$A_N = A_{N-1} + (N-1)A_{N-2}, \qquad N \geqslant 3, \qquad \text{(A1)}$$

and the values for one- and two-photon states are $A_1 = 1$ and $A_2 = 2$.

APPENDIX B: THE SPATIAL SPLIT-STATE DENSITY MATRIX FOR PHOTONS WITH UNCORRELATED FREQUENCY SPECTRA

Although our approach is applicable to arbitrary multiphoton split states, here, we discuss an example with states composed of photons with uncorrelated frequency spectra. Specifically, we consider a pure N-photon state

$$|\Psi\rangle = \int d\omega_0 \, d\omega_1, \, \ldots, d\omega_{N-1} \psi(\omega_0, \omega_1, \ldots, \omega_{N-1}) \hat{a}_0^\dagger(\omega_0) \hat{a}_1^\dagger(\omega_1) \cdots \hat{a}_{N-1}^\dagger(\omega_{N-1})|0\rangle, \qquad \text{(B1)}$$

with the frequency-dependent wave function featuring no correlations between the individual spectra of photons,

$$\psi(\omega_0, \omega_1, \ldots, \omega_{N-1}) = \phi_0(\omega_0)\phi_1(\omega_1) \cdots \phi_{N-1}(\omega_{N-1}). \qquad \text{(B2)}$$

Here, $\phi_j(\omega_j)$ is an individual spectral wave function of the photon coupled to spatial mode number j.

We calculate the $N!$ nonzero elements of the first row of the reduced density matrix for the N-photon split state as

$$\rho_{0,1,\ldots,N-1;s_0,s_1,\ldots,s_{N-1}} = \mathrm{Tr}(\hat{\rho}\,\hat{O}_{0,1,\ldots,N-1;s_0,s_1,\ldots,s_{N-1}})$$

$$= \frac{1}{N!} \int d\omega_0 d\omega_1 \cdots d\omega_{N-1} \phi_0^*(\omega_0)\phi_1^*(\omega_1) \cdots \phi_{N-1}^*(\omega_{N-1}) \phi_{s_0}(\omega_0)\phi_{s_1}(\omega_1) \cdots \phi_{s_{N-1}}(\omega_{N-1}) \qquad \text{(B3)}$$

$$= \frac{1}{N!} I_{0,s_0} I_{1,s_1} \cdots I_{N-1,s_{N-1}},$$

where $(s_0, s_1, \ldots, s_{N-1})$ are permutations in the set $(0, 1, \ldots, N - 1)$ without repetition and we define the spectral overlaps between different photon pairs or the distinguishability function as

$$I_{i,j} = \langle \phi_i | \phi_j \rangle = \int d\omega \phi_i^*(\omega)\phi_j(\omega) = r_{ij}e^{i\theta_{ij}}, \qquad \text{(B4)}$$

with the normalization $I_{j,j} = 1$.

For an $N = 3$ photon case, we have

$$\rho_{0,1,2;0,1,2} = \frac{1}{6}, \quad \rho_{0,1,2;0,2,1} = \frac{1}{6}|I_{1,2}|^2 = \frac{1}{6}r_{12}^2,$$

$$\rho_{0,1,2;1,0,2} = \frac{1}{6}|I_{0,1}|^2 = \frac{1}{6}r_{01}^2, \quad \rho_{0,1,2;2,1,0} = \frac{1}{6}|I_{2,0}|^2 = \frac{1}{6}r_{20}^2,$$

$$\rho_{0,1,2;1,2,0} = \frac{1}{6}I_{0,1}I_{1,2}I_{2,0} = \frac{1}{6}r_{01}r_{12}r_{20}e^{i\theta_{012}},$$

(B5)

$$\rho_{0,1,2;2,0,1} = \frac{1}{6}I_{0,1}^*I_{1,2}^*I_{2,0}^* = \frac{1}{6}r_{01}r_{12}r_{20}e^{-i\theta_{012}},$$

where $\theta_{012} = \theta_{01} + \theta_{12} + \theta_{20}$ is the three-photon collective phase. Note that the definitions of the distinguishability function $I_{i,j}$ and collective phase here are the same as the ones defined in Ref. [15]. Correspondingly, the six free parameters in Fig. 1(d) are

$$\rho_1 = \rho_{0,1,2;0,1,2}, \quad \rho_2 = \rho_{0,1,2;0,2,1}, \quad \rho_3 = \rho_{0,1,2;1,0,2},$$

$$\rho_4 = \text{Re}(\rho_{0,1,2;1,2,0}), \quad \rho_5 = \text{Im}(\rho_{0,1,2;1,2,0}), \quad \rho_6 = \rho_{0,1,2;2,1,0}.$$

(B6)

[1] M. A. Nielsen and I. L. Chuang, *Quantum Computation and Quantum Information*, 10th ed. (Cambridge University Press, Cambridge, 2011).

[2] C. K. Hong, Z. Y. Ou, and L. Mandel, Measurement of Subpicosecond Time Intervals between Two Photons by Interference, Phys. Rev. Lett. **59**, 2044 (1987).

[3] F. Bouchard, A. Sit, Y. W. Zhang, R. Fickler, F. M. Miatto, Y. Yao, F. Sciarrino, and E. Karimi, Two-photon interference: The Hong-Ou-Mandel effect, Rep. Prog. Phys. **84**, 012402 (2021).

[4] A. J. Menssen, A. E. Jones, B. J. Metcalf, M. C. Tichy, S. Barz, W. S. Kolthammer, and I. A. Walmsley, Distinguishability and Many-Particle Interference, Phys. Rev. Lett. **118**, 153603 (2017).

[5] N. Spagnolo, C. Vitelli, L. Aparo, P. Mataloni, F. Sciarrino, A. Crespi, R. Ramponi, and R. Osellame, Three-photon bosonic coalescence in an integrated tritter, Nat. Commun. **4**, 1606 (2013).

[6] D. J. Brod, E. F. Galvao, N. Viggianiello, F. Flamini, N. Spagnolo, and F. Sciarrino, Witnessing Genuine Multiphoton Indistinguishability, Phys. Rev. Lett. **122**, 063602 (2019).

[7] M. Pont, R. Albiero, S. E. Thomas, N. Spagnolo, F. Ceccarelli, G. Corrielli, A. Brieussel, N. Somaschi, H. Huet, A. Harouri, A. Lemaitre, I. Sagnes, N. Belabas, F. Sciarrino, R. Osellame, P. Senellart, and A. Crespi, Quantifying *n*-Photon Indistinguishability with a Cyclic Integrated Interferometer, Phys. Rev. X **12**, 031033 (2022).

[8] T. Giordani, D. J. Brod, C. Esposito, N. Viggianiello, M. Romano, F. Flamini, G. Carvacho, N. Spagnolo, E. F. Galvao, and F. Sciarrino, Experimental quantification of four-photon indistinguishability, New J. Phys. **22**, 043001 (2020).

[9] J. B. Spring, B. J. Metcalf, P. C. Humphreys, W. S. Kolthammer, X. M. Jin, M. Barbieri, A. Datta, N. Thomas-Peter, N. K. Langford, D. Kundys, J. C. Gates, B. J. Smith, P. G. R. Smith, and I. A. Walmsley, Boson sampling on a photonic chip, Science **339**, 798 (2013).

[10] M. A. Broome, A. Fedrizzi, S. Rahimi-Keshari, J. Dove, S. Aaronson, T. C. Ralph, and A. G. White, Photonic boson sampling in a tunable circuit, Science **339**, 794 (2013).

[11] M. Tillmann, B. Dakic, R. Heilmann, S. Nolte, A. Szameit, and P. Walther, Experimental boson sampling, Nat. Photonics **7**, 540 (2013).

[12] A. Crespi, R. Osellame, R. Ramponi, D. J. Brod, E. F. Galvao, N. Spagnolo, C. Vitelli, E. Maiorino, P. Mataloni, and F. Sciarrino, Integrated multimode interferometers with arbitrary designs for photonic boson sampling, Nat. Photonics **7**, 545 (2013).

[13] V. S. Shchesnovich, Tight bound on the trace distance between a realistic device with partially indistinguishable bosons and the ideal boson sampling, Phys. Rev. A **91**, 063842 (2015).

[14] J. J. Renema, A. Menssen, W. R. Clements, G. Triginer, W. S. Kolthammer, and I. A. Walmsley, Efficient Classical Algorithm for Boson Sampling with Partially Distinguishable Photons, Phys. Rev. Lett. **120**, 220502 (2018).

[15] V. S. Shchesnovich and M. E. O. Bezerra, Collective phases of identical particles interfering on linear multiports, Phys. Rev. A **98**, 033805 (2018).

[16] A. E. Jones, A. J. Menssen, H. M. Chrzanowski, T. A. W. Wolterink, V. S. Shchesnovich, and I. A. Walmsley, Multiparticle Interference of Pairwise Distinguishable Photons, Phys. Rev. Lett. **125**, 123603 (2020).

[17] J. B. Altepeter, E. R. Jeffrey, and P. G. Kwiat, Photonic state tomography, Adv. Atom., Mol., Opt. Phys. **52**, 105 (2005).

[18] A. I. Lvovsky and M. G. Raymer, Continuous-variable optical quantum-state tomography, Rev. Mod. Phys. **81**, 299 (2009).

[19] E. Toninelli, B. Ndagano, A. Valles, B. Sephton, I. Nape, A. Ambrosio, F. Capasso, M. J. Padgett, and A. Forbes, Concepts in quantum state tomography and classical implementation with intense light: A tutorial, Adv. Opt. Photonics **11**, 67 (2019).

[20] Y. S. Teo, S. Shin, H. Jeong, Y. Kim, Y. H. Kim, G. I. Struchalin, E. V. Kovlakov, S. S. Straupe, S. P. Kulik, G. Leuchs, and L. L. Sanchez-Soto, Benchmarking quantum tomography completeness and fidelity with machine learning, New J. Phys. **23**, 103021 (2021).

[21] D. F. V. James, P. G. Kwiat, W. J. Munro, and A. G. White, Measurement of qubits, Phys. Rev. A **64**, 052312 (2001).

[22] P. J. Shadbolt, M. R. Verde, A. Peruzzo, A. Politi, A. Laing, M. Lobino, J. C. F. Matthews, M. G. Thompson, and J. L. O'Brien, Generating, manipulating and measuring entanglement and mixture with a reconfigurable photonic circuit, Nat. Photonics **6**, 45 (2012).

[23] G. M. D'Ariano, Universal quantum observables, Phys. Lett. A **300**, 1 (2002).

[24] A. E. Allahverdyan, R. Balian, and T. M. Nieuwenhuizen, Determining a Quantum State by Means of a Single Apparatus, Phys. Rev. Lett. **92**, 120402 (2004).

[25] G. M. D'Ariano, P. Perinotti, and M. F. Sacchi, Quantum universal detectors, Europhys. Lett. **65**, 165 (2004).

[26] J. G. Titchener, A. S. Solntsev, and A. A. Sukhorukov, Two-photon tomography using on-chip quantum walks, Opt. Lett. **41**, 4079 (2016).

[27] L. Banchi, W. S. Kolthammer, and M. S. Kim, Multiphoton Tomography with Linear Optics and Photon Counting, Phys. Rev. Lett. **121**, 250402 (2018).

[28] J. G. Titchener, M. Grafe, R. Heilmann, A. S. Solntsev, A. Szameit, and A. A. Sukhorukov, Scalable on-chip quantum state tomography, npj Quantum Inf. **4**, 19 (2018).

[29] K. Wang, J. G. Titchener, S. S. Kruk, L. Xu, H. P. Chung, M. Parry, I. I. Kravchenko, Y. H. Chen, A. S. Solntsev, Y. S. Kivshar, D. N. Neshev, and A. A. Sukhorukov, Quantum metasurface for multiphoton interference and state reconstruction, Science **361**, 1104 (2018).

[30] V. S. Shchesnovich, Sufficient condition for the mode mismatch of single photons for scalability of the boson-sampling computer, Phys. Rev. A **89**, 022333 (2014).

[31] V. S. Shchesnovich, Partial indistinguishability theory for multiphoton experiments in multiport devices, Phys. Rev. A **91**, 013844 (2015).

[32] D. N. Christodoulides, F. Lederer, and Y. Silberberg, Discretizing light behaviour in linear and nonlinear waveguide lattices, Nature (London) **424**, 817 (2003).

[33] J. H. Zhou, J. J. Wu, and Q. S. Hu, Tunable arbitrary unitary transformer based on multiple sections of multicore fibers with phase control, Opt. Express **26**, 3020 (2018).

[34] N. N. Skryabin, I. V. Dyakonov, M. Y. Saygin, and S. P. Kulik, Waveguide-lattice-based architecture for multichannel optical transformations, Opt. Express **29**, 26058 (2021).

[35] R. Garcia-Patron, J. J. Renema, and V. Shchesnovich, Simulating boson sampling in lossy architectures, Quantum **3**, 169 (2019).

[36] W. R. Clements, P. C. Humphreys, B. J. Metcalf, W. S. Kolthammer, and I. A. Walsmley, Optimal design for universal multiport interferometers, Optica **3**, 1460 (2016).

[37] Y. Lahini, G. R. Steinbrecher, A. D. Bookatz, and D. Englund, Quantum logic using correlated one-dimensional quantum walks, npj Quantum Inf. **4**, 2 (2018).

[38] A. Szameit, F. Dreisow, M. Heinrich, T. Pertsch, S. Nolte, A. Tunnermann, E. Suran, F. Louradour, A. Barthelemy, and S. Longhi, Image reconstruction in segmented femtosecond laser-written waveguide arrays, Appl. Phys. Lett. **93**, 181109 (2008).

[39] M. Y. Saygin, I. V. Kondratyev, I. V. Dyakonov, S. A. Mironov, S. S. Straupe, and S. P. Kulik, Robust Architecture for Programmable Universal Unitaries, Phys. Rev. Lett. **124**, 010501 (2020).

[40] B. A. Bell, G. S. Thekkadath, R. Y. Ge, X. L. Cai, and I. A. Walmsley, Testing multi-photon interference on a silicon chip, Opt. Express **27**, 35646 (2019).

[41] G. R. Steinbrecher, J. P. Olson, D. Englund, and J. Carolan, Quantum optical neural networks, npj Quantum Inf. **5**, 60 (2019).

[42] W. H. Press, S. A. Teukolsky, W. T. Vetterling, and B. P. Flannery, *Numerical Recipes: The Art of Scientific Computing*, 3rd ed. (Cambridge University Press, Cambridge, 2007).

[43] K. Wang, S. V. Suchkov, J. G. Titchener, A. Szameit, and A. A. Sukhorukov, Inline detection and reconstruction of multiphoton quantum states, Optica **6**, 41 (2019).

[44] Z. Wang, T. T. Li, A. Soman, D. Mao, T. Kananen, and T. Y. Gu, On-chip wavefront shaping with dielectric metasurface, Nat. Commun. **10**, 3547 (2019).